Mesoscopic Simulation of Dendritic Growth Observed in X-ray Video Microscopy During Directional Solidification of Al–Cu Alloys

Pierre DELALEAU,[1,2)] Christoph BECKERMANN,[1)] Ragnvald H. MATHIESEN[3)] and Lars ARNBERG[2)]

1) Department of Mechanical and Industrial Engineering, University of Iowa, Iowa City, IA 52242, USA.
2) Department of Materials Science and Engineering, NTNU, N-7491 Trondheim, Norway
3) Department of Physics, NTNU, N-7491 Trondheim, Norway.

A mesoscopic model is developed to simulate microstructures observed *in situ* by X-ray video microscopy during directional solidification of Al–Cu alloys in a Hele–Shaw cell. In the model, a volume-averaged species conservation equation is solved to obtain the solute concentration and solid fraction fields, and an analytical stagnant film model is used to predict the motion of the dendrite envelopes. The model is carefully validated in several test cases. Then, the model is applied to simulate the columnar dendritic microstructures observed in the X-ray video microscopy experiments for two different alloy compositions. Reasonable agreement is found between the measured and predicted dendrite envelope shapes, solid fractions, and solute concentration fields. The predicted size of the mushy zone and the extent of the undercooled melt region ahead of the columnar front agree well with the *in situ* experimental observations. The simulation results show quantitative agreement with the internal solid fraction variations measured from the radiographs. The present model is also able to realistically simulate a primary dendrite trunk spacing adjustment that was observed in one of the experiments. Overall, the present study represents the first successful validation of a solidification model using real time, in situ data from an experiment with a metallic alloy. Considerable additional research is needed to account in the model for the effect of gravity driven melt convection.

KEY WORDS: mesoscopic simulation; directional solidification; Al–Cu alloys.

1. Introduction

Recently, X-ray imaging techniques have emerged as an ideal tool for observing solidification microstructure evolution in metal alloys.[1–11)] These methods provide the opportunity to monitor the development of the microstructure in real time and *in situ*. They can be used to obtain spatio-temporally resolved measurements of growth morphologies, solid fraction distributions, solute concentration fields, and melt flow patterns. The number of X-ray imaging studies reported in the solidification literature has increased steadily over the last decade, but until now no attempt has been made to simulate the actual microstructure evolution observed in such experiments.

Dendrites are the most common growth form observed during solidification of metal alloys. Dendritic growth is governed by an intricate interplay between diffusion of heat and solute, capillarity, and thermophysical properties, which combine to span a wide range of length and time scales.[12,13)] Due to this complexity, analytical theories are limited to a single isolated dendrite tip growing into an infinite undercooled melt.[12,14)] However, significant advances have been made to numerically simulate dendritic growth. The most commonly used computational models are the cellular-automaton (CA) technique[15,16)] and the phase-field (PF) method.[17–19)]

To directly simulate the microstructures observed in X-ray imaging experiments, a three-dimensional PF model would require excessive computational resources. The original CA model by Gandin and Rappaz[15,16)] could be used to simulate the growth of multiple dendrites on the scale of the experiments, but it does not resolve the solute concentration field between the dendrites. The modified CA technique by Zhu and Hong[20)] appears to offer a compromise between these two models, but suffers from an inconsistent calculation of the solid fraction directly from the dendrite tip growth rate instead of from an interfacial solute balance. Another compromise is provided by the so-called mesoscopic modelling approach originally developed by Steinbach *et al.*[21,22)] This model combines a meso-scale numerical solution of the relevant transport equations with a micro-scale analytical solution for dendrite tip growth. Since the original mesoscopic model was limited to dendritic growth of a pure substance, it is extended here to solidification of a binary alloy with a prescribed temperature field. The extended mesoscopic model is used in the present study to simulate previously performed X-ray imaging experiments involving directional solidification of

Al–Cu alloys.

2. Model and Governing Equations

The present model for dendritic solidification of a binary alloy combines an analytical description of dendrite tip growth with a numerical solution of a volume-averaged solute conservation equation. The temperature field is prescribed, and melt convection and solid movement are neglected. Central to the model is the definition of a virtual grain (or dendrite) envelope. As illustrated in **Fig. 1**, the grain envelope is a smooth surface that connects all actively growing dendrite tips. Thus, the normal propagation velocity at any point on the envelope is given by the local dendrite tip growth velocity and the angle of the growing dendrite arm with respect to the envelope normal. The melt on the envelope surface as well as inside of the grain envelope is assumed to be well-mixed and in equilibrium with the adjacent solid. The actual structure of the dendritic solid inside of the envelope is not resolved in the model; instead, a local solid volume fraction, g_s, is defined that gives the volume of solid per unit volume of solid plus liquid at a point, in an ensemble- or volume-averaged sense. The extra-dendritic liquid outside of the grain envelope is generally undercooled. The solute concentration field, C_l, in the extra-dendritic liquid is obtained from a numerical solution of the solute conservation equation. Hence, the solutal interactions between the growing grains are fully resolved. Overall, the model thus consists of a solute conservation equation and an envelope propagation algorithm.

The volume-averaged solute conservation equation is given by

$$g_l \frac{\partial C_l}{\partial t} = D_l \nabla \cdot (g_l \nabla C_l) + C_l(k-1)\frac{\partial g_l}{\partial t} \quad \text{.........(1)}$$

where $g_l = 1 - g_s$ is the liquid volume fraction, t is time, D_l is the solute diffusivity in the liquid, and k the equilibrium partition coefficient. In Eq. (1), the solid and liquid densities are assumed to be equal and constant, the liquid solute diffusivity is assumed to be constant, and solute diffusion in the solid is neglected. The latter assumption implies that $d(g_s C_s) = kC_l dg_s$, where C_s is the volume-averaged solute concentration of the solid.

Equation (1) is valid everywhere in the domain, both inside of the grain envelope and in the extra-dendritic liquid. Outside of the envelope, $g_l = 1$ and Eq. (1) becomes a standard transient diffusion equation that is solved for C_l. Inside of the envelope, the liquid is assumed to be in equilibrium with the solid, such that C_l is given by the liquidus concentration, C_l^*, *i.e.*,

$$C_l\big|_{\text{envelope}} = C_l^*(T) = C_0 + \frac{T - T_{\text{liq}}}{m} \quad \text{..............(2)}$$

where T is the prescribed temperature, T_{liq} is the liquidus temperature of the alloy, C_0 is the initial solute concentration of the alloy, and m is the slope of the liquidus line. T_{liq}, m, and k are obtained from the equilibrium phase diagram of the binary alloy under consideration. With C_l known as a function of T, Eq. (1) is solved inside of the envelope for the liquid fraction, g_l. Note that without the first term on the right-hand side (*i.e.*, the diffusion term), Eq. (1) is nothing
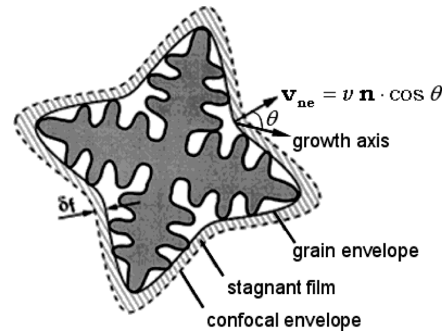

Fig. 1. Illustration of the grain envelope, the stagnant film and the confocal envelope.[21]

but the differential form of the Scheil equation. However, in the presence of undercooled extra-dendritic liquid, the diffusion term is non-zero at the envelope surface. Hence, the liquid fraction is affected by solute diffusion from the envelope into the extra-dendritic liquid and is not just equal to the Scheil value.

Next, the envelope propagation algorithm is described. As mentioned previously, the envelope evolves due to growth of dendrite tips. The local dendrite tip growth velocity, v, is obtained as a function of the local melt undercooling across a so-called stagnant film. As illustrated in Fig. 1, the stagnant film is bounded on one side by the grain envelope and on the other side by a confocal envelope. The stagnant film is of a constant width, δ_f. The dimensionless melt undercooling, Ω_{sf}, across the stagnant film is given by

$$\Omega_{sf} = \frac{C_l^* - C_{ce}}{C_l^*(1-k)} \quad \text{...........................(3)}$$

where C_{ce} is the local liquid solute concentration on the surface of the confocal envelope. For the concentrated alloys considered in the present study, thermal undercooling can safely be neglected. Curvature undercooling and kinetic effects are negligibly small as well. The local solute concentration on the confocal envelope is known from the solution of Eq. (1) in the extra-dendritic liquid, which can expressed as

$$C_{ce} = C_l\big|_{\delta_f} \quad \text{..................................(4)}$$

Knowing the melt undercooling across the stagnant film, a dendrite tip growth Péclet number, Pe, is obtained from the modified Ivantsov solution of Cantor and Vogel[23]

$$\Omega_{sf} = \text{Pe} \exp(\text{Pe}) \left[E_1(\text{Pe}) - E_1\left(\text{Pe}\left(1 + 2\frac{\delta_f}{R} \right) \right) \right] \quad \text{...(5)}$$

where E_1 is the exponential integral function and R is the dendrite tip radius. The Péclet number is defined as $\text{Pe} = vR/(2D_l)$ and, thus, contains the desired dendrite tip growth velocity, v. The final unknown is the dendrite tip radius, and it is obtained from the LGK[14] model according to

$$R = \frac{1}{2\text{Pe}} \frac{\Gamma}{\sigma^* C_0 m(k-1)} \quad \text{.....................(6)}$$

where Γ is the Gibbs–Thomson coefficient and $\sigma^* = (2\pi)^{-2}$ is a stability constant.[24] Equations (5) and (6) provide an implicit relation for the dendrite tip growth velocity as a function of the melt undercooling across the stagnant film,

i.e., $v(\Omega_{sf})$. An explicit version of this relation was found by curve fitting. In a simulation of dendritic growth, the dendrite tip growth velocity will vary along the grain envelope, because the melt undercooling across the stagnant film is generally not uniform.

With the local dendrite tip growth velocity at any point on the envelope known, the normal envelope propagation velocity is determined from

$$\mathbf{v}_{ne} = v\mathbf{n}\cos\theta \qquad (7)$$

As illustrated in Fig. 1, **n** is the exterior normal to the envelope and θ is the angle between **n** and the growth axis of the nearest dendrite arm. In a simulation, each grain is seeded with a specific crystallographic orientation. Assuming that the primary and secondary dendrite arms grow at right angles to each other, the direction of the growth axis of the dendrite arms can then be determined. The calculation of **n** is explained below.

In order to propagate the envelope on a fixed numerical mesh, the sharp interface tracking method recently developed by Sun and Beckermann[25] is employed. In this method, an indicator function, φ, is introduced that varies smoothly in a hyperbolic tangent fashion from $+1$ to -1 across the interface. An interface is represented by a contour of φ. The indicator function is advected with the normal envelope velocity using the following propagation equation

$$\frac{\partial\varphi}{\partial t} + |\mathbf{v}_{ne}|\|\nabla\varphi\| = 0.5\left[\nabla^2\varphi + \frac{\varphi(1-\varphi^2)}{W^2} - |\nabla\varphi|\nabla\cdot\left(\frac{\nabla\varphi}{|\nabla\varphi|}\right)\right]$$

$$\qquad (8)$$

where W is a measure of the width of the hyperbolic tangent profile across the interface. While the left-hand-side of Eq. (8) advects any function normal to its contour, the right-hand-side maintains the hyperbolic tangent φ profile across the interface. The distance over which φ changes from 0.9 to -0.9 is constant and given by $3\sqrt{2}W$. As shown in **Fig. 2**, the grain envelope is taken to be the $\varphi=0.9$ contour, while the confocal envelope is represented by the $\varphi=0$ contour. Thus, the width of the stagnant film is related to W by $3\sqrt{2}W=2\delta_f$. Finally, the envelope normal vector is given by $\mathbf{n}=-\nabla\varphi/|\nabla\varphi|$.

Before the above mesoscopic model can be solved, the width of the stagnant film, δ_f, needs to be specified. In fact, δ_f is the only adjustable parameter, and the results should ultimately be independent of δ_f, since it is not a physical quantity. The choice of δ_f is discussed in detail in Steinbach *et al.*[21,22] Since the micro-scale solute concentration field in the liquid adjacent to individual dendrite tips is not resolved by the solution of the volume-averaged solute conservation equation, δ_f must generally be larger than the tip radius. Due to solutal interactions between dendrites, δ_f should be much smaller than the distance between them. Without this separation of length scales, the present model would not work. As is shown below, a stagnant film width can be found that gives results that are independent of δ_f for a reasonably wide range of growth velocities.

Since the present experiments were performed in a Hele–Shaw cell with a relatively small gap thickness (see Chap. 4 below), the mesoscopic solute concentration field
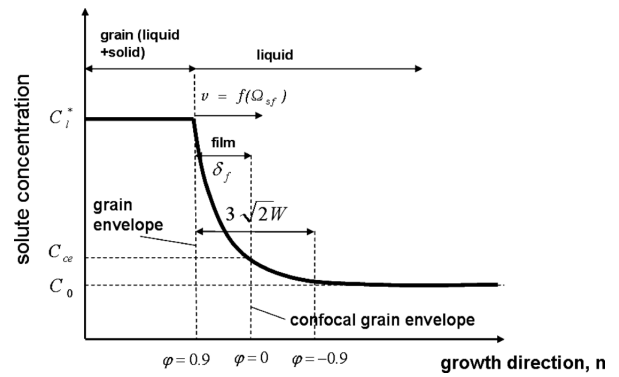

Fig. 2. Schematic of the liquid solute concentration profile normal to a grain envelope.

Table 1. Properties for Al–Cu alloys used in the simulations.

Property	Value		Units
initial concentration, C_0	20	30	wt%
liquidus temperature, T_{liq}	875.5	836.4	K
solute diffusivity, D_l	2.5×10^{-9}	2×10^{-9}	m²/s
equilibrium partition coefficient, k	0.12	0.15	-
slope of the liquidus line, m	-3.55	-4.6	K/wt%
Gibbs–Thomson coefficient, Γ	2.4×10^{-7}	2.4×10^{-7}	Km

is assumed to be uniform across the gap. Therefore, Eqs. (1) and (8) are solved in two dimensions (x,y) only. In all simulations, the computational domain is a $1\,300\times1\,300$ mm² square, which corresponds to the field of view in the experiments. The equations are solved numerically using a uniform, square mesh with a grid size of dx. Equation (1) is discretized using an explicit finite-difference scheme with a second-order, 9-point stencil in space.[25] Once discretized, it is solved for the new liquid solute concentration at the mesh points that are located outside of the envelope (with $g_l=1$), and for the new liquid fraction at the mesh points that are located inside of the envelope (with $C_l=C_l^*(T)$). Equation (8) is discretized using the high-order method explained in Sun and Beckermann.[25] In order to maintain sufficient numerical resolution of the φ field, all simulations employ $W=2dx$. All calculations were performed on a personal computer and took generally less than 1 h to complete.

3. Validation

Before the mesoscopic model is applied to simulate the experiments, it is tested and validated for three different cases that all involve dendritic solidification of an Al–Cu alloy with an initial concentration of $C_0=20$ wt% Cu. The thermo-physical properties used in the simulations are listed in **Table 1**.

3.1. Growth of a Single Dendrite in an Undercooled Melt

The first test case concerns steady growth of a single equiaxed dendrite in an essentially infinite, uniformly undercooled melt. The melt undercooling is set to

$\Omega = (C_l^* - C_0)/(C_l^*(1-k)) = 0.1$. **Figure 3** shows the results of two simulations with $dx = 5\,\mu$m, at a time of 5 s after initialization. In the first simulation the primary growth axes of the centred seed were aligned with the coordinate axes, while in the second simulation the growth axes were rotated by 45°. Essentially the same results are obtained (see also **Fig. 4** below), which indicates that the numerical scheme used does not suffer from grid anisotropy effects. As can be seen from Fig. 3, the grain envelope (white line) develops a typical dendrite shape. Solute diffuses outwardly from the envelope into the undercooled melt. The solid fraction field shows several interesting features. The small red dot in the centre represents the initial seed. Over most of the grain, the solid fraction is approximately equal to 0.2. However, along the primary growth axis, the solid fraction is somewhat above 0.2, which can be attributed to enhanced solute transport at the envelope in the tip region.

Figure 4 shows computed steady-state dendrite tip growth velocities as a function of the undercooling. Numerous simulations were performed to find a suitable value for the width of the stagnant film, δ_f. Figure 4 shows the results for $\delta_f = 21.2\,\mu$m and $10.6\,\mu$m. For dimensionless undercoolings up to 0.1, this range of film widths gives consistent tip velocities that are fairly close to each other. Much smaller or much larger δ_f do not give reasonable results. It can also be seen that the computed tip velocities are close to the analytical result from the LGK[14] model, which is given by Eqs. (5) and (6) with $\delta_f \to \infty$. The two results cannot be expected to be identical because in the present simulations, the extra-dendritic solute concentration is only computed in two dimensions. Nonetheless, the differences are not large, since in the mesoscopic model the tip velocities are calculated from essentially the same equations as in the LGK model (except for the stagnant film width). To better compare the mesoscopic model with the LGK model, fully three-dimensional simulations are required. Such a validation was successfully performed in the original study by Steinbach et al.[21] They also found that the predicted envelope shape behind the tip matches experimental measurements.

3.2. Growth of a Cylinder in an Undercooled Melt at Constant Velocity

In order to validate the computation of the solid fraction inside of the envelope, a second test case was designed that allows for a semi-analytical solution to be found. In this case, the two-dimensional growth of an infinite dendritic cylinder in a uniformly undercooled melt was simulated. Instead of calculating the growth velocity from the equations for a dendrite, it was taken as a constant, denoted by v_n. In analogy with the heat balance in Ref. 26), the variation of the average solid volume fraction, $\bar{g}_s$, inside of the growing cylinder can be obtained from a solute balance,

$$\frac{d}{dt}(\bar{g}_s V) = AD_l \frac{\Omega}{\delta} \qquad \ldots\ldots\ldots\ldots\ldots(9)$$

where V and A are the cylinder volume and surface area, respectively, and δ is the thickness of the solutal boundary layer around the cylinder. For a constant growth velocity, this thickness can be obtained from an analytical solution of the solute diffusion equation for a growing cylinder, using

the method explained in Ref. 27), and is given by

$$\delta = \frac{D_l}{v_n}[\mathrm{Pe}_n E_1(\mathrm{Pe}_n)\exp(\mathrm{Pe}_n)] \qquad \ldots\ldots\ldots\ldots(10)$$

where $\mathrm{Pe}_n = v_n R/D_l$, in which R is the instantaneous cylinder radius ($R = v_n t$). By substituting Eq. (10) into Eq. (9) and performing some rearrangements, one obtains the following ordinary differential equation for the average solid fraction

$$\frac{t}{2}\frac{d\bar{g}_s}{dt} + \bar{g}_s = \Omega[\mathrm{Pe}_n E_1(\mathrm{Pe}_n)\exp(\mathrm{Pe}_n)]^{-1} \quad \ldots\ldots(11)$$

The initial condition was taken to be a small seed with $\bar{g}_s = 1$. The solution of Eq. (11) is shown in **Fig. 5**(b).

Figure 5 shows the mesoscopic simulation results for this case with $\Omega = 0.1$ and $v_n = 50\,\mu$m/s. The predicted solute concentration field shows a thin boundary layer around the cylinder. The predicted evolution of the average solid fraction is plotted in Fig. 5(b). Excellent agreement with the solution of Eq. (11) is obtained. The solid fraction decreases from the initial value of unity and asymptotically approaches a value of 0.1. It can easily be seen from Eq. (11) that $\bar{g}_s = \Omega$ is indeed the long-time analytical result.

3.3. One-dimensional Directional Solidification

The last test case concerns one-dimensional directional solidification, in which a fixed vertical (in y) temperature gradient, G, is translated across the domain with a constant "pulling" speed, v_p. Thus, the temperature distribution is given by

$$T = G(y - y_0) + T_{\mathrm{liq}} \qquad \ldots\ldots\ldots\ldots\ldots(12)$$

where y is as the vertical coordinate and y_0 is the y-position of the T_{liq} isotherm. A moving domain technique[28] is employed to simulate the translation of the temperature gradient across the domain. The domain is moved at discrete time intervals dx/v_p by shifting all fields by one grid point along y, removing the top row while introducing a new row of points at the bottom. The new points are initialized as liquid with $C_l = C_0$.

The results of a simulation with $G = -20\,$K/mm and $v_p = 50\,\mu$m/s are shown in **Fig. 6**. In this simulation, the liquidus isotherm is located at the bottom of the domain (i.e., $y_0 = 0$) and the temperature decreases (linearly) toward the top. Thus, solidification proceeds in a downward direction. Figure 6(a) shows the predicted quasi-steady solute concentration field in the liquid, C_l. The envelope is located at about $y = 440\,\mu$m. Above the envelope, inside of the dendritic mushy zone, C_l varies in a linear fashion, in accordance with Eq. (2). Below the white line, in the liquid ahead of the dendritic front, a steep concentration gradient can be observed where the liquid concentration quickly approaches C_0. Since the liquidus temperature is at the bottom of the domain, the entire liquid below the envelope is constitutionally undercooled.

Figure 6(b) shows the computed solid fraction, g_s, profile. Inside of the mushy zone, the solid fraction varies in agreement with the Scheil equation, $g_s = 1 - (C_l/C_0)^{1/(k-1)}$. At the position of the envelope, the predicted solid fraction abruptly decreases to zero. This variation is in accordance with the so-called truncated Scheil model, which has been verified through direct phase-field simulations to be an

excellent approximation for columnar dendritic solidification of an alloy.[28]

4. Simulation of Experiments

4.1. Experimental Setup

The experimental data selected for simulation by the mesoscopic model were taken from two *in situ* X-ray video microscopy sequences of columnar dendritic growth during directional solidification of an Al–20wt%Cu alloy and of an Al–30wt%Cu alloy.[2] The experiments were carried out at beamline ID22 at the European Synchrotron Radiation Facility, under experiment codes HS-1332 and ME-595. The Al–Cu alloy was contained inside of a Hele–Shaw cell, which consists of two closely spaced quartz glass plates. The gap thickness was $\Delta z_{sample} = 200$ mm, while the lateral dimensions of the cell were 12×22 mm^2. The Hele–Shaw cell was placed inside a Bridgman furnace system and translated upward towards the cold stage at a constant velocity, v_p. The imposed temperature gradient, G, was set by adjusting the furnace separation distance and operating temperatures, and was verified to be approximately constant, at least over the imaging region. In both test sequences the camera settings employed gave a field of view of 1.3×1.3 mm^2, with nominal temporal and spatial resolutions of 0.15 s and 1.3 μm, respectively. Hence, the imaging region was about 150 times smaller than the Hele–Shaw cell. Further details of the experimental procedure and setup, as well as a description of high-energy synchrotron X-ray imaging, can be found elsewhere.[1]

4.2. Internal Solid Fraction Measurements

In order to quantitatively compare the experimental data with the simulations, an attempt was made to measure solid volume fractions from the radiographic images. This can only be done in an approximate fashion, since the radiographs are two-dimensional projections of a complex, three-dimensional, confined microstructure. A typical radiograph from one of the experiments is shown in **Fig. 7**(a). The overall goal of the measurements is to obtain the variation of the horizontally averaged solid fraction inside of a dendrite envelope, $\bar{g}_s$, with vertical distance along the primary dendrite axis. For this purpose, an idealized dendrite was constructed from a variety of connected cylinders, as illustrated in Fig. 7(b). The diameter and length of each of the cylinders is estimated by measuring the following microstructural quantities from a radiograph: primary trunk diameter, D_{trunc}, secondary arm diameter, D_{arm}, secondary arm length, L_{arm}, and secondary arm spacing, λ_2. All of these quantities vary with distance along the primary dendrite axis. Since the secondary arms that are growing in the z direction, parallel to the incident X-ray beam, cannot be seen on the radiograph, their diameter and length are assumed to be the same as the adjacent secondary arms that are growing in the image plane. However, since the dendrite is confined inside of the Hele–Shaw cell, the length of the secondary arms growing in the z direction is restricted by requiring that $D_{trunc} + 2L_{arm} < \Delta z_{sample}$. As sketched in Fig. 7(b), the internal solid fraction is then calculated for a parallelepiped volume, V_0, that has a height equal to λ_2 and an average rectangular cross section that spans the tips of the secondary arms. One parallelepiped volume thus contains five cylinders, and the sum of their volumes is the total solid volume, V_s, within V_0. The internal solid fraction is then given by $\bar{g}_s = V_s / V_0$.

4.3. Comparison between Simulation and Experimental Results

The first experiment involves directional solidification of an Al–20wt%Cu alloy with $G = -18$ K/mm and $v_p = 10.5$ μm/s. **Figure 8**(a) shows a typical image from the video of this experiment. Three columnar dendrites are visible in the field of view. In this image, the system has reached a quasi-steady state, meaning that the positions of the three primary dendrite tips are fixed in the field of view. This occurs only if the primary axes of the dendrites are aligned with the direction of the temperature gradient, as is the case in the image. Note, however, that the spacing between the dendrites is very different.

This experiment was simulated by placing three properly oriented seeds at the upper boundary of the $1\,300 \times 1\,300$ μm^2 simulation domain, applying the temperature gradient and moving domain technique of Sec. 3.3, and letting the system evolve for a long time. The position of the liquidus isotherm was estimated based on temperature measurements to be at $y_0 \approx 350$ μm. No-flux boundary conditions were applied at the left and right sides of the domain, and the grid spacing was chosen to be $dx = 5$ μm.

Figures 8(b) and 8(c) show the predicted results after the system reaches a quasi-steady state. Remarkable agreement is achieved between the predicted dendrite envelope shapes and the overall shape of the dendrites in the experiment. In the experimental image, the Cu content of the melt is approximately visible as different gray levels. These gray levels compare well, in a qualitative sense, with the predicted liquid solute concentration field (Fig. 8(b)). The predicted solid fraction field (Fig. 8(c)) shows some non-uniformities inside of the envelopes, which also appear to correspond well with the solid microstructure that can be observed in the experimental image.

The measured internal solid fractions, $\bar{g}_s$, for dendrites 1 and 2 (see Fig. 8(a)) are plotted in **Fig. 9** as a function of distance along the primary dendrite axes (*i.e.*, the y direction). The error bars on the symbols denote the estimated measurement uncertainty. These measurements are compared in Fig. 9 with the simulation results for this experiment. The variation of the internal solid fraction in the simulation was obtained by averaging the predicted solid fraction field along a horizontal line that spans across the envelope (see Fig. 8(c)). Excellent agreement can be observed. The internal solid fraction is relatively uniform along the dendrite axes, with values around 0.25, except near the primary dendrite tips where it increases to higher values. This can be expected because the melt undercooling is largest near the primary tips and the secondary arms become very short. Also shown in Fig. 9 (as a black line) is the solid fraction prediction from the Scheil equation. The Scheil solid fractions are generally below the measured and predicted internal solid fractions. This is expected because the Scheil model predicts a solid fraction that is averaged over both the solid–liquid mixture inside of the envelopes and the liquid between the envelopes. Furthermore, it does not
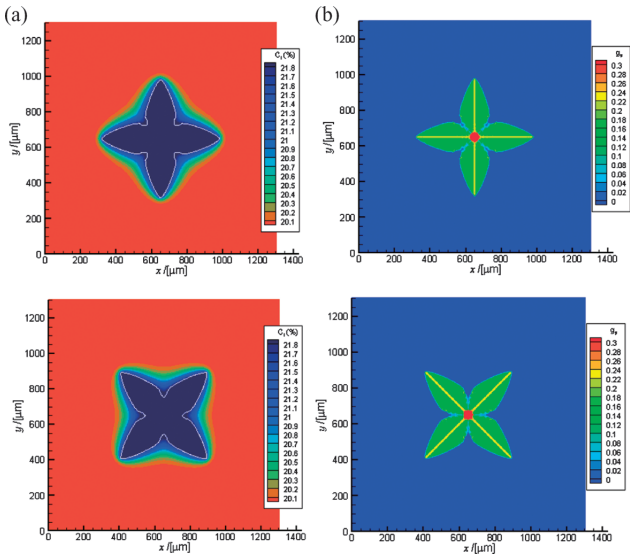
Fig. 3. Predicted envelope shape (white line) and solute concentration field (colours) (a) and solid fraction field (b) for a single equiaxed dendrite of an Al–20wt%Cu alloy growing into a uniformly undercooled melt (Ω=0.1). The upper panels are for a dendrite with the growth axes aligned with the coordinate axes, while the lower panels are for a dendrite with the growth axes rotated by 45°.
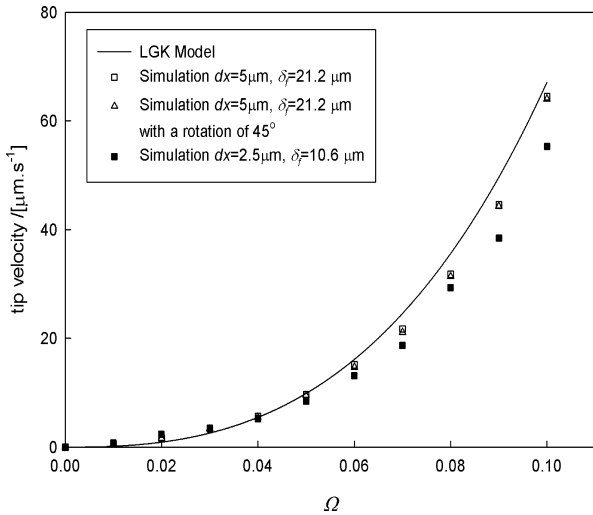

Fig. 4. Effect of different grid sizes and grain orientations on the predicted tip velocities for a single equiaxed dendrite of an Al–20wt%Cu alloy. The mesoscopic model predictions for different melt undercoolings (symbols) are compared to the LGK model (line).
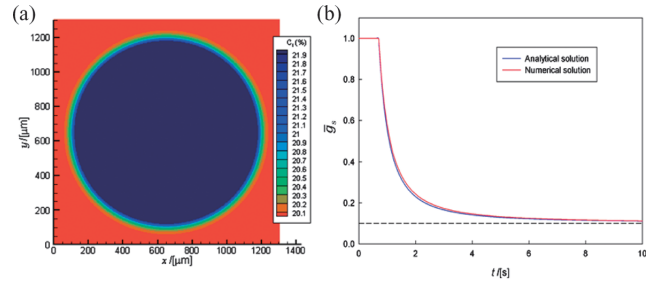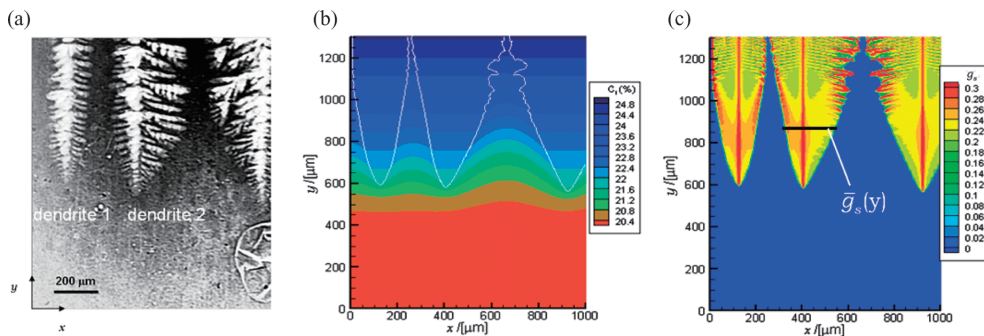

Fig. 5. Predicted liquid solute concentration field for an infinite cylinder growing into a uniformly undercooled melt at constant velocity (Al–20wt%Cu, Ω=0.1, v_n=50 μm/s) (a), and comparison of the predicted average solid fraction with an analytical solution (b).
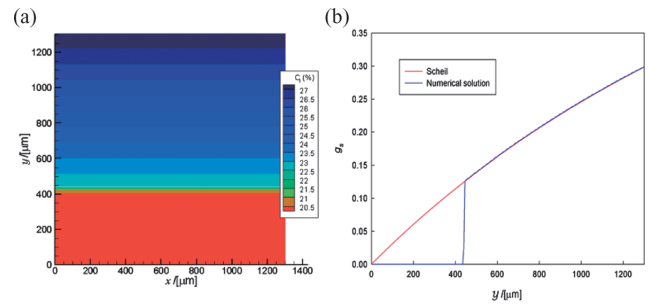
Fig. 6. Predicted liquid solute concentration field for one-dimensional directional solidification of an Al–20wt%Cu alloy (G=−20 K/mm, v_p=50 μm/s) (a), and comparison of the predicted solid fraction variation with the Scheil equation (b).
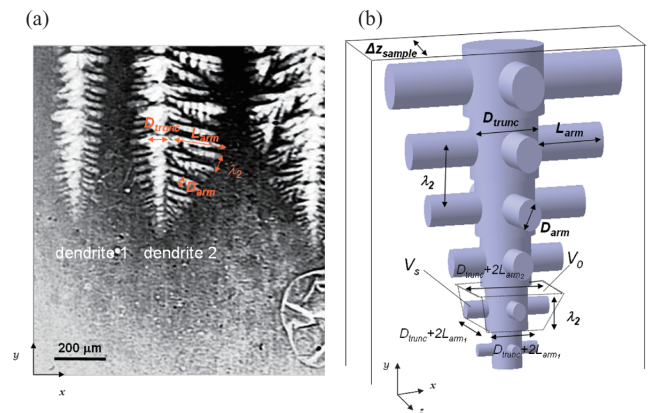
Fig. 7. Illustration of the measurements made to determine the internal solid fraction from the experimental images (a), and idealized dendrite geometry used to calculate the internal solid fraction (b).

Fig. 8. Comparison of results for directional solidification of an Al–20wt%Cu alloy with G=−18 K/mm and v_n=10.5 μm/s: (a) radiographic image from the experiment, (b) predicted grain envelopes and liquid solute concentration field, (c) predicted solid fraction field.

take undercooling of the liquid into account. The mesoscopic model predictions and the measured internal solid fractions approach the Scheil curve toward the top of the domain ($y=1\,300$ mm), where the envelopes meet and there is no more extra-dendritic liquid (see Fig. 8(b)).

The second experiment involves an Al–30wt%Cu alloy that is directionally solidified with $G=-27$ K/mm and $v_p=22.4\,\mu$m/s. The high Cu content combined with the high thermal gradient results in a very shallow mushy zone. As can be seen from the experimental image in **Fig. 10**(a), the primary dendrite tips and the eutectic front are present simultaneously in the field of view. For a binary alloy, the eutectic front corresponds to an isotherm. It can be seen in Fig. 10(a) that the eutectic front is not completely horizontal, which indicates that the temperature gradient was slightly inclined. Furthermore, the four dendrites visible in the image are not completely aligned with the temperature gradient. In particular, the third and fourth dendrites from the left appear to be slightly misoriented. The image in Fig. 10(a) does not correspond to a full quasi-steady state and the temperature field and the solid microstructure are still evolving (see the experimental images in **Fig. 11** below). The colours in the images of this experiment indicate the approximate Cu content of the melt. In principle, quantitative solute concentration fields can be extracted from the experimental data,[2] but in the images of the present experi-

ment they are only of a qualitative nature. Nonetheless, a solutal boundary layer can be observed in the melt ahead of the columnar front. The solute concentration increases from the original alloy composition (30 wt% Cu) far ahead of the dendrites to the eutectic composition (33.2 wt% Cu) near the eutectic front.

In order to simulate the second experiment, a temperature field was prescribed that matches at all times the location and inclination of the eutectic front observed in the experiment. In addition to applying a vertical temperature
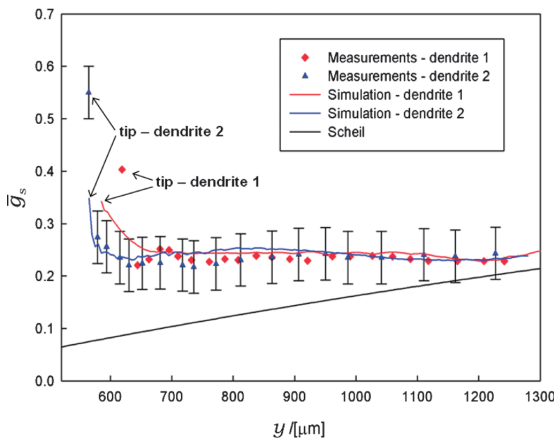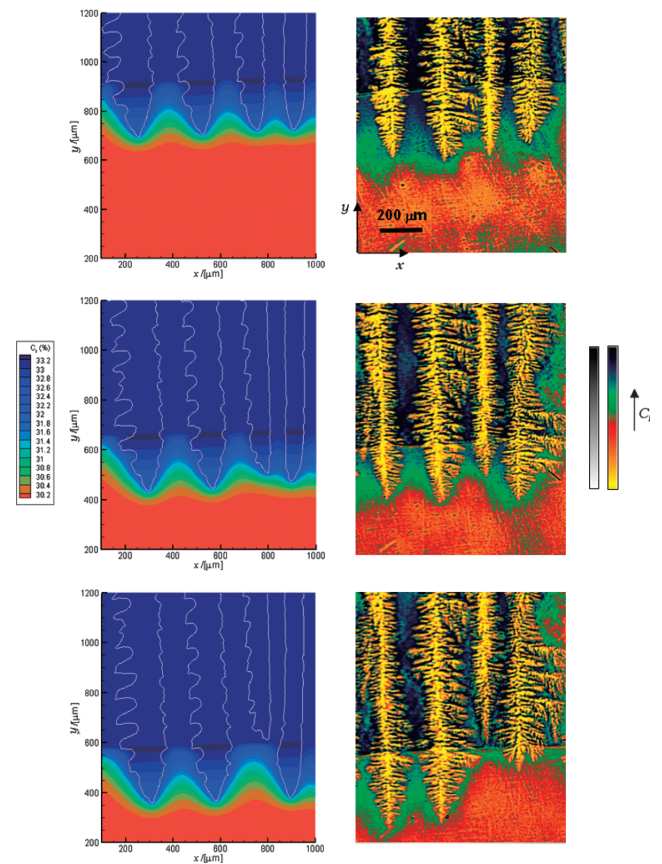

Fig. 11. Comparison of a time sequence of measured and predicted results for directional solidification of an Al–30wt%Cu alloy with $G=-27$ K/mm and $v_n=22.4$ μm/s, showing overgrowth and elimination of a primary dendrite branch (time increasing from top to bottom). Left panels: predicted grain envelopes and liquid solute concentration fields; right panels: radiographic images from the experiment. Bar charts to the right relate the colour table used in the radiograhs to grey levels.
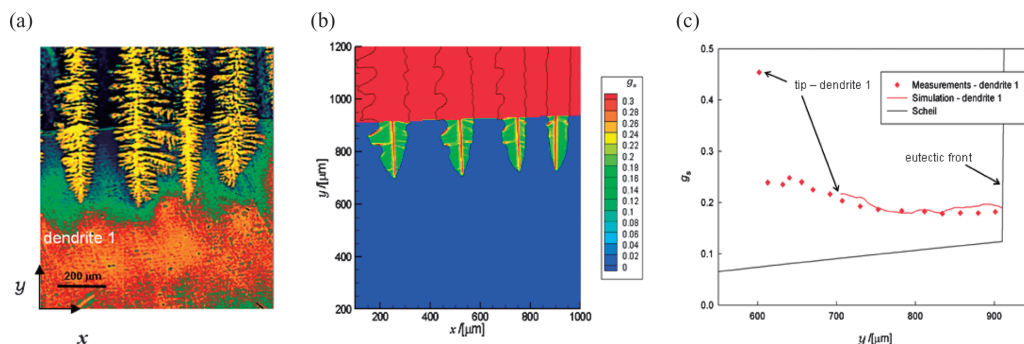

Fig. 9. Comparison of measured and predicted internal solid fraction variations for directional solidification of an Al–20wt%Cu alloy with $G=-18$ K/mm and $v_p=10.5$ μm/s, and corresponding prediction from the Scheil equation.

Fig. 10. Comparison of results for directional solidification of an Al–30wt%Cu alloy with $G=-27$ K/mm and $v_p=22.4$ μm/s: (a) radiographic image from the experiment, (b) predicted solid fraction field and (c) measured and predicted internal solid fraction variations together with the corresponding prediction from the Scheil equation.

gradient of $G_y = -27$ K/mm, a small horizontal temperature gradient of $G_x = +2$ K/mm[2)] was imposed to model the inclination. Furthermore, the reference temperature in Eq. (12) was chosen to be the eutectic temperature and y_0 was continually adjusted to match the average height of the eutectic front in the X-ray video of the experiment. In order to model the formation of the eutectic, the liquid solute concentration was set to the eutectic concentration at the location of the eutectic isotherm and the solid fraction to unity behind the eutectic front. The simulation was initialized by placing four seeds at the top of the domain, such that the lateral positions and orientations of the four dendrites in the experimental image are closely matched.

Figure 10(b) shows the predicted solid fraction field for this experiment at a time when the eutectic front is at approximately $y = 925 \, \mu$m. Reasonably good agreement is obtained with the experimental image in Fig. 10(a). At the eutectic front, there is still a considerable amount of undercooled liquid present between the dendrite envelopes. Hence, as shown in Fig. 10(c) for the left-most dendrite, the solid fraction never approaches the Scheil prediction. Figure 10(c) shows that the measured and predicted internal solid fractions agree well over the entire (predicted) length of this dendrite. The main disagreement between the measured and predicted results is in the position of the columnar front. In the experimental image (Fig. 10(a)), the primary tips of the dendrites are located at about $y = 600 \, \mu$m, while the predicted position is at approximately $y = 700 \, \mu$m (Fig. 10(b)). While this difference is small in absolute terms (0.1 mm), it may indicate inaccuracies in the dendrite tip growth model used in the mesoscopic model, including uncertainties in the stability constant. A more likely reason, however, is the effect of melt convection in the experiment. The X-ray video of this experiment clearly shows the presence of melt flow. The flow advects solute past the primary dendrite tips and thus modifies their growth. This is discussed in more detail below.

Figure 11 shows a time sequence of simulation results and X-ray images, where the third dendrite (from the left) is overgrown by the neighbouring dendrites and eventually gets eliminated and "captured" by the eutectic front. The elimination process occurs because there is a slight misorientation between the third and fourth dendrite. Note that the eutectic front moves downward during this sequence, indicating that the temperature had not reached a steady state. As already explained, this was realized in the simulation by continually adjusting the imposed temperature gradient. Not surprisingly, the measured and predicted eutectic front locations agree almost perfectly. Figure 11 shows that, overall, the elimination process of the third dendrite is simulated well.

Figure 11 also allows for a qualitative comparison of the measured and predicted liquid solute concentration fields over time. At first glance, the agreement appears to be reasonably good. However, upon closer inspection one finds considerable differences. The red colour indicates a Cu concentration equal to the initial melt concentration of 30 wt%Cu, while the dark blue colour corresponds to the eutectic concentration of 33.2 wt%. In the first experimental image, the entire range of colours is present in the liquid between the dendrites. However, at the two later times, the dark blue liquid near the eutectic front has largely disappeared. As was confirmed by the X-ray video of this experiment, this is the result of solutally driven melt convection. Since the density of a liquid Al–Cu alloy increases with increasing Cu concentration, a melt layer with a higher Cu content above one with a lower Cu content is a hydrodynamically unstable situation. As a result, the Cu rich melt close to the eutectic front flows downward in the form of periodic plumes and is replaced by melt of a lower Cu content (with a green colour in Fig. 11). This effect is particularly strong in the present experiment because of the wide open spaces between the dendrites and the short vertical extent of the mushy zone. The unsteady melt convection also causes variations in the dendrite growth velocity.[2)] This can be observed in the experimental images in Fig. 11 by noting that the length of the first and second dendrites, between the eutectic front and the primary tips, is not the same in the three images. Similar fluctuations in the growth velocity due to unsteady melt convection were recently found in two-dimensional phase-field simulations of columnar dendritic growth.[19)]

In addition to the solutally driven melt convection, there is evidence of large-scale thermal convection in the experimental X-ray video sequence. This flow is from the right to the left of the field of view.[2)] It can be discerned in Fig. 11 by noting that the waves in the solutal boundary layer near the columnar front are sometimes shifted relative to the dendrites. The presence of thermal convection in the experiments is not surprising, since the present Bridgman setup is thermally unstable (cold at the top, hot at the bottom) and there are some heat losses from the sides of the Hele–Shaw cell. It is believed that the inclination of the eutectic front is also evidence of large-scale thermal convection.

Since the present simulations do not include melt flow, the agreement between the measured and predicted results in Fig. 11 is limited. An attempt was made to include convection in the simulations, but it was unsuccessful so far, primarily due to our inability to specify realistic boundary conditions for the flow at the edges of the simulation domain. In order to fully predict the flow, a much larger simulation domain, equal in size to the entire Hele–Shaw cell, is needed. This will be attempted in the near future.

5. Conclusions

Synchrotron X-ray video microscopy experiments involving directional solidification of Al–Cu alloys are simulated using a mesoscopic model. The mesoscopic model is an extension of the purely thermal model of Steinbach et al.,[21,22)] and is valid for columnar and equiaxed dendritic solidification of alloys with a prescribed temperature field. It uses an averaged solute conservation equation together with a dendrite tip growth model for the propagation of the grain/dendrite envelopes. The model is extensively validated in three different test cases. It is then used to simulate the columnar dendritic growth occurring during the X-ray video experiments. For both alloy compositions, reasonably good agreement is obtained between measured and predicted dendrite envelope shapes and internal solid fractions, despite the neglect of melt convection. This indicates that the model correctly predicts the solute concentration field

in the extra-dendritic liquid. The predicted height of the mushy zone and extent of the undercooled melt region ahead of the columnar front both agree with the experimental observations. The present authors are not aware of another study where such predictions are verified for a solidifying metallic alloy. It is also shown that a primary trunk spacing adjustment observed in one of the experiments, due to a misorientation between dendrites, can be realistically simulated. The comparison of the instantaneous solid fraction fields also constitutes the first successful validation of such a prediction for a metallic alloy. The differences to the Scheil model are emphasized. Considerable additional research is necessary. In particular, the effect of gravity driven melt flow needs to be investigated further. The inclusion of melt convection in the present mesoscopic model is possible, but a much larger computational domain will be needed.

Acknowledgements

REFERENCES

1) R. H. Mathiesen, L. Arnberg, K. Ramsøskar, T. Weitkamp, C. Rau and A. Snigirev: *Metall. Mater. Trans. B*, **33B** (2002), 613.
2) R. H. Mathiesen and L. Arnberg: *Acta Mater.*, **53** (2005), 947.
3) R. H. Mathiesen, L. Arnberg, P. Bleuet and A. Somogyi: *Metall. Mater. Trans. A*, **37** (2006), 2515.
4) L. Arnberg and R. H. Mathiesen: *JOM*, **59** (2007), No. 8, 20.
5) T. Schenk, H. N. Thi, J. Gastaldi, G. Reinhart, V. Cristiglio, N. Mangelinck-Noel, H. Klein, J. Hartwig, B. Grushko, B. Billia and J. Baruchel: *J. Cryst. Growth*, **275** (2005), 201.
6) H. Nguyen-Thi, G. Reinhart, N. Mangelinck-Noel, H. J. H, B. Billia, T. Schenk, J. Gastaldi, J. Hartwig and J. Baruchel: *Metall. Mater. Trans. A*, **38A** (2007), 1458.
7) H. Yasuda, I. Ohnaka, K. Kawasaki, A. Sugiyama, T. Ohmichi, J. Iwane and K. Umetani: *J. Cryst. Growth*, **262** (2004), 645.
8) H. Yasuda, Y. Yamamoto, N. Nakatsuka, M. Yoshiya, T. Nagira, A. Sugiyama, I. Ohnaka, K. Uesugi and K. Umetani: *Int. J. Cast Met. Res.*, **22** (2009), 15.
9) S. Boden, S. Eckert, B. Willers and G. Gerbeth: *Metall. Mater. Trans. A*, **39A** (2008), 613.
10) G. Reinhart, A. Buffet, H. Nguyen-Thi, B. Billia, H. Jung, N. Mangelinck-Noel, N. Bergeon, T. Schenk, J. Hartwig and J. Baruchel: *Metall. Mater. Trans A*, **39A** (2008), 865.
11) H. Jung, N. Mangelinck-Noel, H. Nguyen-Thi, N. Bergeon, B. Billia, A. Buffet, G. Reinhart, T. Schenk and J. Baruchel: *Int. J. Cast Met. Res.*, **22** (2009), 208.
12) R. Trivedi and W. Kurz: *Int. Mater. Rev.*, **39** (1994), 49.
13) M. B. Amar and P. Pelcé: *Phys. Rev. A*, **39** (1989), 4263.
14) J. Lipton, M. E. Glicksman and W. Kurz: *Mater. Sci. Eng.*, **65** (1984), 57.
15) C.-A. Gandin and M. Rappaz: *Acta Metall. Mater.*, **42** (1994), 2233.
16) C.-A. Gandin and M. Rappaz: *Acta Mater.*, **45** (1997), 2187.
17) A. Karma and W.-J. Rappel: *J. Cryst. Growth*, **174** (1997), 54.
18) I. Steinbach: *Model. Simul. Mater. Sci. Eng.*, **17** (2009), 073001.
19) I. Steinbach: *Acta Mater.*, **57** (2009), 2640.
20) M. F. Zhu and C. P. Hong: *ISIJ Int.*, **41** (2001), 436.
21) I. Steinbach, C. Beckermann, B. Kauerauf, Q. Li and J. Guo: *Acta Mater.*, **47** (1999), 971.
22) I. Steinbach, H.-J. Diepers and C. Beckermann: *J. Cryst. Growth*, **275** (2005), 624.
23) B. Cantor and A. Vogel: *J. Cryst. Growth*, **14** (1977), 109.
24) J. S. Langer and H. Muller-Krumbhaar: *J. Cryst. Growth*, **42** (1977), 11.
25) Y. Sun and C. Beckermann: *J. Comput. Phys.*, **220** (2007), 626.
26) Q. Li and C. Beckermann: *Phys. Rev. E*, **57** (1998), 3176.
27) M. A. Martorano, C. Beckermann and C.-A. Gandin: *Metall. Mater. Trans. A*, **34A** (2003), 1657.
28) A. Badillo and C. Beckermann: *Acta Mater.*, **54** (2006), 2015.